Evaluation of commercial Virtually Imaged Phase Array and Fabry-Pérot based Brillouin spectrometers for applications to biology

Guqi Yan, Antony Bazir, Jérémie Margueritat, Thomas Dehoux

▶ To cite this version:

HAL Id: hal-02922474

https://hal.archives-ouvertes.fr/hal-02922474

Submitted on 26 Aug 2020

Evaluation of commercial Virtually Imaged Phase Array and Fabry-Pérot based Brillouin spectrometers for applications to biology

GUQI YAN,[1] ANTONY BAZIR,[1] JEREMIE MARGUERITAT,[1] AND THOMAS DEHOUX[1,*]

[1]*Institut Lumière Matière, UMR5306, Université Lyon 1-CNRS, Université de Lyon, 69622 Villeurbanne, France*
[*]*thomas.dehoux@univ-lyon1.fr*

Abstract: Measuring the complex mechanical properties of biological objects has become a necessity to answer key questions in mechanobiology and to propose innovative clinical and therapeutic strategies. In this context, Brillouin light scattering (BLS) has recently come into vogue, offering quantitative imaging of the mechanical properties without labels and with a micrometer resolution. In biological samples, the magnitude of the spectral changes are typically of a few tens of MHz, and the ability of modern spectrometers to monitor such subtle changes needs to be evaluated. Moreover, the multiplicity of variations in optical arrangements, specific to each lab, requires to set a standard for the assessment of the characteristics of BLS systems. In this paper we propose a protocol to evaluate the precision and accuracy of two commercial spectrometers that is reproducible across labs. For a meaningful comparison, we coupled the spectrometers to the same microscope and to the same laser. We first evaluated the optimum acquisition time and laser power. We evaluated the precision using pure water samples. We determined the accuracy by probing water solutions with increasing concentration of salt and comparing with theory. Following these quantifications, we applied the VIPA-based spectrometer to tumor spheroids engineered from different cell lines that possess different metastatic potentials and resistance to therapies. On these models, we detected significant changes in the linewidth suggesting that BLS measurements of the viscosity could be used as read-out to distinguish different level of drug resistance.

1. Introduction

The mechanical phenotype of cells and tissues has been recognized as a marker for developmental stage [1], also ensuring unaltered development of tissues [2] and regulating the response to therapeutic agents [3]. For this, measuring the complex mechanical properties of biological objects, often exhibiting behaviors reminiscent of soft glasses [4] or poroelastic materials [5], has become a necessity to answer key questions in mechanobiology and to propose innovative clinical and therapeutic strategies [6]. In this context, many techniques have been implemented, mostly inherited from material science, such as atomic force microscopy [7, 8] or rheometers [9], to extract Young or shear modulus in the static to sub-kHz range. In these techniques, a contact to the sample or the use of labels is usually required. Recently, Brillouin light scattering (BLS) has come into vogue, offering quantitative imaging of the complex longitudinal modulus without labels and with a micrometer resolution [10].

BLS has been used recently to image the mechanical properties of single cells using spectroscopic [11] and time-resolved implementations [12], live organisms [13], plant tissues [14], teeth [15] or tumor spheroids [16]. In BLS, the infinitesimal compressive motion induced by the spontaneous acoustic phonons creates a periodic grating of refractive index fluctuations. Using a monochromatic visible light beam, this grating with a spacing imposed by the acoustic wavelength

produces a peak in the spectrum of the backscattered light characterized by a frequency shift f and a full width at half maximum Γ.

Measuring such spectral features that typically lie in the GHz range (i.e. $\sim$ 0.3 cm^{-1} wavenumber shift) requires spectrometers that greatly filter the contribution of elastic scattering (i.e. with a high rejection of Rayleigh scattering), and today two main technologies contend. The first is based on the analysis of the scattered light by a 6-pass Fabry-Pérot (FP) etalon [17], and offers a contrast as high as 150 dB [18], but often results in long acquisition times due to the scanned design. The second technology, known as virtually imaged phased array (VIPA) [19], relies on the analysis of a beam focused onto a fixed etalon, resulting in the angular dispersion of the spectrum that can then be recorded by a CCD array. Altough this solution offers a much lower contrast (typically ~80 dB), it enables acquisition times shorter than 0.1 ms, making it particularly attractive for high-throughput applications [20].

In biological samples, the magnitude of the spectral changes are typically of tens to a few hundreds of MHz, and the ability of modern spectrometers to monitor such subtle changes needs to be evaluated. Moreover, the multiplicity of variations in optical arrangements, specific to each lab, requires to set a standard for the assessment of the characteristics of BLS systems. In a recent paper [21], the impact of the acquisition time on the precision of BLS measurements has been investigated in acetone. However the impact of laser power and other external conditions have not been detailed, and the accuracy (i.e. the closeness of the data to the true value) was not measured. In this paper we propose a protocol to evaluate the precision and accuracy of two commercial spectrometers that is reproducible across labs.

For a meaningful comparison, we coupled the spectrometers to the same microscope and to the same laser. We first evaluated the optimum acquisition time and laser power. We evaluated the precision using pure water samples. We determined the accuracy by probing water solutions with increasing concentration of salt and comparing with theory. Following these quantifications, we applied the VIPA-based spectrometer to tumor spheroids engineered from different cell lines.

2. Materials and methods

2.1. Brillouin spectroscopy

Brillouin light scattering (BLS) is an inelastic process [22] arising with creation (Stokes process) or annihilation (anti-Stokes process) of acoustic phonons in the medium. The resulting spectra consist of peaks shifted by frequencies $\pm \nu_B$ (the '+' and '−' signs correspond to the anti-Stokes and Stokes contributions, respectively) relative to the frequency of the incident laser light. The Brillouin frequency shift, ν_B, and the full width at half maximum (FWHM) of the peak, Γ_B, are defined by the following relations [23]:

$$\nu_B = \frac{1}{2\pi} qV,\tag{1}$$

$$\Gamma_B = \frac{1}{2\pi}\frac{4}{3}\frac{\eta}{\rho}q^2,\tag{2}$$

where $q = 4n\pi/\lambda$ is the optical wavevector, V the acoustic velocity, n the refractive index, λ the laser wavelength and η the viscosity.

Solving the Navier-Stokes equation for a non-conductive liquid in the low-frequency regime ($\ll$ 1 THz) yields the acoustic attenuation [24]

$$\alpha = \frac{2\omega^2 \eta}{3\rho V^3},\tag{3}$$

which is essentially Stokes' law, with $\omega = 2\pi\nu_B$, the angular frequency. When introducing α into Eq. 2 we obtain the expression
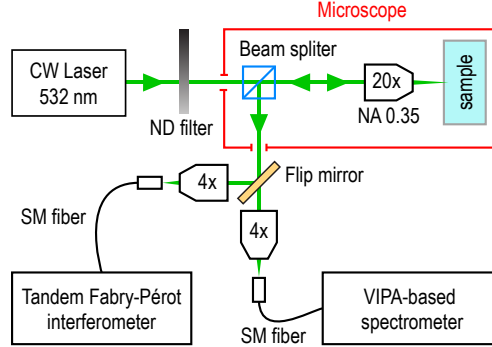
$$\Gamma_B = \alpha V/\pi\tag{4}$$

Fig. 1. Experimental setup showing the coupling of the VIPA-based and Fabry-Pérot interferometers with the life science microscope.

that shows that the linewidth does not depend on the laser wavelength λ.

2.2. Coupling Fabry-Pérot and VIPA-based interferometer

To make an unbiased comparison between the two types of spectrometers we used in this work, it is necessary to use the same laser. We used a 532-nm single mode CW laser with a spectral linewidth < 0.01 pm (Spectra-Physics Excelsior-532). The laser is coupled to an inverted life-science microscope (Nikon Eclipse Ti2-U) to focus and collect the backscattered light with the same objective lens (20×, N.A. 0.35). We chose a lens with a low numerical aperture to avoid broadening of the Brillouin spectrum [16]. The direction of the output beam is controlled by a flip mirror (see Fig. 1), and collected by identical objective lenses (4×, N.A. 0.10) into two identical single-mode (SM) fibres (1 meter, 400-680 nm, diameter 125 μm). One fiber is connected to the VIPA-based spectrometer and the other one is connected to the Fabry-Pérot-based spectrometer. To ensure perfect control of the sample, the microscope is enclosed in an environmental chamber to maintain a constant temperature and, in the case of biological samples, 5% CO_2 level. During the measurements, a temperature sensor is placed next to the sample inside the chamber, in order to analyze the influence of the temperature variation.

2.3. Commercial spectrometers

Two commercial spontaneous Brillouin instruments are used in this work, a scanning multi-pass tandem Fabry-Pérot interferometers (TFPI [17] JRS Scientific Instruments) and a VIPA-based spectrometer (Light Machinery, Hyperfine HF-8999-532). The TFPI is equipped with two sets of mirrors with 95% reflectivity, and an avalanche photodiode (Count®Blue, Laser Components) with a dark count lower than 10 counts/s (typically 2 counts/s) and a quantum efficiency of 70% at 532 nm. An optical setup that matches the numerical aperture of the TFPI and of the single-mode fiber has been built to connect the TFPI to the fiber. The VIPA spectrometer is based on a 3.37 mm thick VIPA etalon (30 GHz, 500 nm to 600 nm), and is equipped with two double passed air spaced etalons (named Green-Killer) to increase the contrast to about 120 dB. The fiber is directly connected to the built-in FC/PC connector of the VIPA spectrometer. The free spectral range (FSR) of the VIPA used in our work is 30 GHz, corresponding to a sampling interval of 0.11 GHz. We therefore fixed the FSR to 30 GHz and reduced the number of the scanning channels of the TFPI from 1024 (maximum value available) to 256, in order to obtain a similar sampling interval (0.10 GHz). The reduction of the number of channels also decreases the duration of each scanning cycle of the TFPI, allowing a reliable comparison of the acquisition

times with the VIPA instrument.

2.4. Data analysis

Before the fitting procedure, we verify that the average noise (measured in the spectral regions without any Brillouin peaks) is zero. Assuming a moderate attenuation in our systems, we fit the spectra with a Lorentzian function (a damped harmonic oscillator might be more suited in highly attenuating samples) [25]:

$$L(f) = L_0 \Gamma_{raw}/2\pi[(\nu - \nu_B)^2 + (\Gamma_{raw}/2)^2]. \tag{5}$$

where L_0 is the maximum intensity of the spectrum and Γ_{raw} is the unprocessed full-width at half maximum. Note that, for the VIPA-based spectrometer, Γ_{raw} results from the convolution (i.e. the Fourier space product) of the experimental linewidth, Γ_B, with the instrument response function (IRF), leading to an overestimation of linewidth by the fitting procedure. Considering that the Brillouin spectra in the sample we probed and the IRF are similar to Lorentzian distributions (see typical spectrum in Fig. 3), we can approximate the deconvolution to a linear deconvolution using the formula:

$$\Gamma_B = \Gamma_{measured} - \Gamma_{IRF}, \tag{6}$$

where Γ_{IRF} is the FWHM of the IRF. Here we measured Γ_{IRF} = 0.792 GHz from the peak of the unsaturated 532 nm single mode CW laser signal. Note that there is no need for such deconvolution with the TFPI spectrometer.

2.5. Cell culture and reagents

HT-29 colorectal adenocarcinoma (HTB-38) and HCT-116 colorectal carcinoma (CCL-247) adenocarcinoma cell lines were purchased from the American Type Culture Collection (ATCC, Virginia, USA). All cell lines were cultured in Dulbecco's Modified Eagle's medium (DMEM-Glutamax), supplemented with 10% of heat-inactivated fetal bovine serum (FBS; Sigma, St. Louis, Missouri, US) and 100 units/100 μg of penicillin/streptomycin. All cells were used at low passage numbers and subconfluently cultured and plated at 10^4 cells per cm^2. The cells were trypsinized and diluted to a concentration of 2400 cells/mL in order to obtain a single spheroid per well, with a diameter at the end of the experimentation not exceeding 300 μm to avoid the formation of a necrotic core. We used Ultra Low Attachment (ULA) 96-wells non-adhesive round-bottom plates (Greiner bio-one) to avoid cell-substrate attachment. The plate is then placed in a humidified atmosphere containing 5% (vol/vol) CO_2 at 37°C for 2 days.

3. Results

3.1. Evaluation of the precision in ultrapure water

In this section we evaluate the precision, that we defined as the standard deviation (SD) of repetitive measurements on the same sample. We used water because it is commonly used as a calibration sample for biological measurements [14, 26–28]. To obtain a sample that can be reproduced in different labs and used as a reference, we purified the water with a Milli-Q® machine. We investigate the two main factors that can influence the amplitude of Brillouin spectra: the acquisition time and the laser power (measured at the sample).

First, in order to study the influence of the acquisition time, we set the laser power to 15 mW and then chose different acquisition times for the two spectrometers. For the VIPA-based spectrometer the acquisition time is defined by the exposure time of the camera. For the TFPI, it is defined by the number of cycles (i.e. the sequence to scan the etalons over the set FSR). To obtain the Brillouin frequency shift ν_B and linewidth Γ_B, we fit the Stokes and anti-Stokes peaks to a Lorentzian function (see **Methods**). For each acquisition time and each spectrometer, we
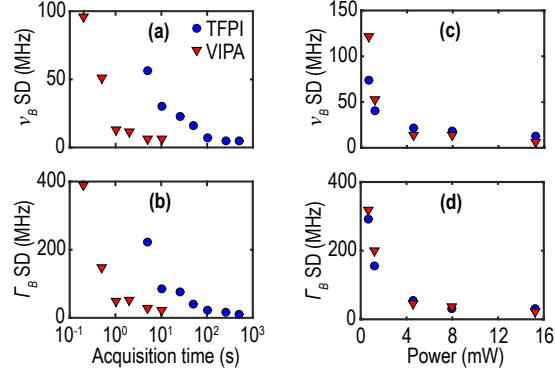
Fig. 2. Standard deviation (SD) vs. acquisition time for Brillouin frequency shift (a) and linewidth (b), and vs. laser power for Brillouin frequency shift (c) and linewidth (d), in ultrapure water. The solid blue squares and the solid red triangles represent for measurements obtained with the TFPI and VIPA-based spectrometers, respectively.

repeated the measurements 10 times. We plot the calculated SD of the ν_B and Γ_B distributions in Figs. 2(a) and 2(b), respectively. The results obtained with the VIPA-based spectrometer (noted as VIPA, red triangles) and with the TFPI (noted as TFPI, blue circles) plotted on Fig. 2(a-b) show that the SD for both the ν_B and Γ_B distributions decrease with increasing acquisition time, as expected. Both systems converge to a precision of $\sim$ 5 MHz for ν_B and $\sim$ 20 MHz for Γ_B. However, the VIPA precision converges more rapidly, meaning that in the same experimental conditions, the VIPA-based spectrometer is about 50 times faster than the TFPI.

For this reason, to study the influence of the laser power, we set the acquisition time to 5 s for the VIPA-based spectrometer and to 256 s for the TFPI. The power is increased gradually by introducing neutral density filters of decreasing density on the beam path before the beam splitter (see Fig. 1). Here too the SD decrease with increasing laser power. This time however the precisions of both VIPA and TFPI instruments superimpose [see Fig. 2(c-d)], confirming the previous results on the acquisition time.

In order to propose a master curve that would simply define the precision of the spectrometers, consider that the decrease of the precision arises from an increase of the ratio between the Brillouin peak amplitude and the background optical noise, i.e. the signal to noise ratio (SNR). We define the SNR as follows:

$$\text{SNR} = 20 \times \log_{10} \left[\text{RMS}(A_{\text{peaks}}) / \text{RMS}(A_{\text{noise}}) \right],$$

where A_{peaks} corresponds to the average amplitude of the Stokes and anti-Stokes peaks (see typical spectrum obtained with the VIPA-based spectrometer in Fig. 3). Note that the amplitudes of the Stokes and anti-Stokes peaks are not exactly the same due to a slight misalignment of the two Green-Killers. A_{noise} is the RMS value of the noise evaluated in a spectral region separated from the Brillouin peaks (see inset in Fig. 3).

We plot again the ν_B and Γ_B precisions shown in Fig. 2, but this time against the SNR determined for each spectrum in Figs. 4(a) and 4(b), respectively. We observe that the precisions evaluated when varying the acquisition time and laser power all superimpose. This master curve is inversely proportional to the square root of the SNR (dashed line in Fig. 4), as expected from the litterature [29]:

$$\text{SD}_{\nu_B, \, \Gamma_B} \propto \frac{1}{\sqrt{\text{SNR}_{\nu_B, \, \Gamma_B}}}. \tag{7}$$
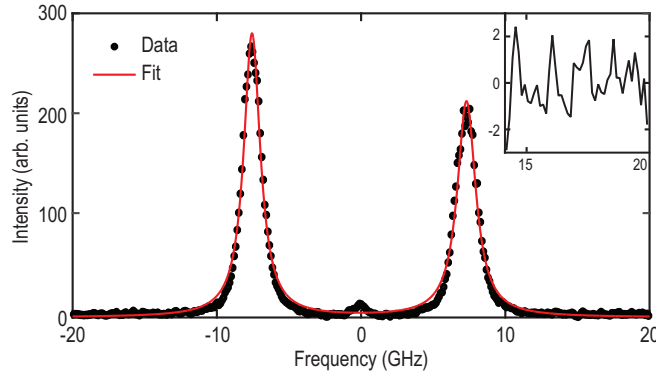
Fig. 3. Determination of the signal-to-noise ratio (SNR): (a) Typical Brillouin spectrum (solid circles) of pure water measured with the VIPA-based spectrometer at room temperature, and fitted (red line) to Lorentzian functions. Inset: zoom-in on spectral regions containing only noise.
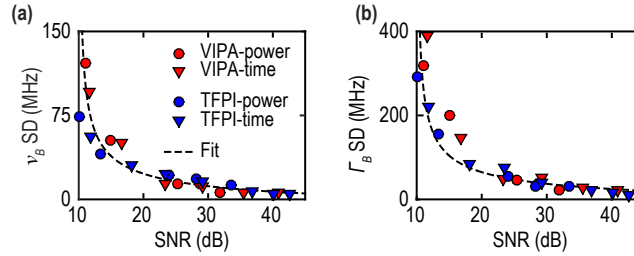

Fig. 4. Standard deviation (SD) of (a) Brillouin frequency shift and (b) linewidth as a function of the corresponding signal to noise ratio (SNR), measured by VIPA-based spectrometer (red markers) and by TFPI (blue markers) and by varying the acquisition time (triangles) and laser power (circles), respectively.

This result suggests that, to evaluate the precision of a BLS interferometer, only the mention of the SNR measured for a given experimental arrangement (power, acquisition time) is required.

3.2. Evaluation of the accuracy using saline solutions

To set the true value, we prepared saline solutions with increasing concentrations of salt, from 0 wt% (pure water) to 20 wt% with step of 4 wt%. In line with the study in Sec. 3.1, to obtain a good precision that is comparable for both spectrometers, we set the laser power to 15 mW, and the acquisition time to 5 s for the VIPA-based spectrometer and 256 s for the TFPI. For each sample of a given concentration, we recorded 10 spectra.

Considering the longer duration of 10 measurements by the TFPI (about 1 hour) compared to the VIPA-based spectrometer (about 1 min), it is necessary to check that the experimental conditions, in particular the temperature, have not changed during the experiment. For this reason, we performed two series of 10 measurements with the VIPA-based spectrometer, the first one before the TFPI measurements (noted as VIPA1) and the second one after the TFPI measurements (noted as VIPA2). A sensor is placed next to the sample (see Methods) to record the temperature each 10 seconds during the experiment (about six hours in total). Figure 5 shows the evolution of the temperature during the experiment. To estimate the impact of such variations, consider that the sound velocity in water varies linearly with temperature by 2.8 m/s/K [30]. Using Eq. 1, we calculate the expected variation in the frequency shift and add in Fig. 5 the corresponding scale
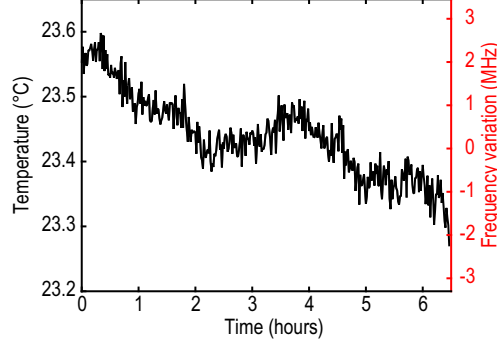
Fig. 5. Room temperature (left *y*-axis) measured during the BLS experiment of saline solutions and corresponding frequency variations (right *y*-axis) estimated for the pure water solution.

(red color). We observe the $\sim 0.3°$C variation leads to about 5 MHz variation in ν_B during the whole experiment.

The frequency shift for the saline solutions of different concentrations are shown in Fig. 6(a). We observe a linear increase of the frequency shift with increasing salt concentration c. To investigate this, we calculate the theoretical shift using Eq. (1). The speed of sound V is a linear function of the salt concentration at 23.4°C [31]:

$$V(c, T) = V_0(T) + a(T) \cdot c, \tag{8}$$

with V_0 and a the speed of sound in pure water and the proportionality factor, respectively. For $T = 23.4°$C, $V_0 = 1492.32 \, m/s$ (averaged value from the Refs. [30] and [32]), and $a = 11.328$ m/s (calculated with the 2nd order polynomial coefficients in Ref. [31]). The refractive index n also depends on salinity and temperature. To take this into account, we used the empirical formula [33]

$$n = 1.3373 + 1.77^{-3}c - 5.8^{-6}c^2 - 1.35^{-4}T - 5.1^{-8}T^2 \tag{9}$$

The frequency ν_B^{th} calculated from these equations is plotted in Fig. 6(a) (dashed line); we observe very good agreement.

The corrected values Γ_B (deconvolving by the instrument response function for the VIPA measurements, see Methods) are shown in Fig. 6(c). To determine the theoretical values for η, we use the data points found in Ref. [35] and fit these to a second order polynomial:

$$\eta = 1.023 + 0.386 \cdot c + 12.32 \cdot c^2 \tag{10}$$

We use this expression to calculate Γ^{th} from Eq. 2. Note that the measured linewidth also contains a term that is due to broadening by the microscope optics Γ_{br}. We fit $\Gamma_{br} + \Gamma_{th}$ to our data by setting $\Gamma_{br} = 321.95$ MHz [see dotted line in Fig. 6(c)]. We observe good agreement between the measurement and theory.

To scrutinize this, we plot the absolute difference between the data, ν_B and Γ_B, and the theoretical values ν_{th} and Γ_{th} defined above for the VIPA and TFPI measurements in Figs. 6(b) and Figs. 6(d). We define the accuracy of the frequency shift and of the linewidth (noted as ν_{acc} and Γ_{acc}, respectively) as the root-mean-square error (RMSE) between the experimental results
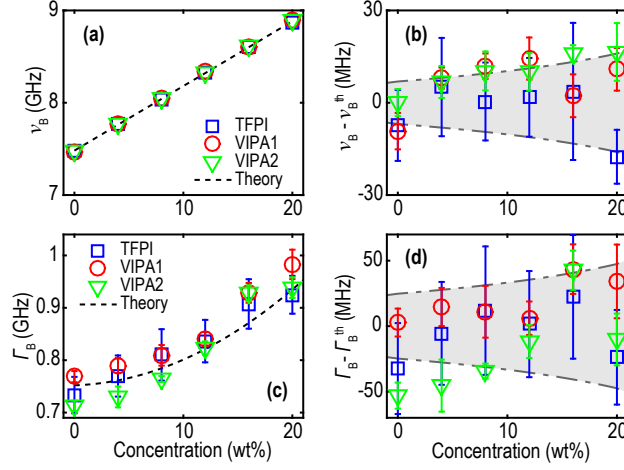
Fig. 6. Experimental results of the evaluation of the VIPA-based spectrometer and the TFPI using the saline solutions: (a) experimental Brillouin frequency shifts (blue cubes corresponds to TFPI, and red circles and green triangles correspond to VIPA results before and after TFPI) with comparison to theory (gray dashed line) V.S. different saline concentrations; (b) absolute differences calculated between the results and the theory; (c) Brillouin linewidth as a function of saline concentrations, gray dashed line represents the best fit by the Eq. (6) in Ref. [34]; (d) the absolute differences (unit MHz) between the results measured by TFPI and those measured by VIPA-based spectrometer before (red circles) and after (green triangles) TFPI measurements, with estimated precision by gray dash-dot lines.

and the theoretical values ν_{th} and Γ_{th} for all the concentrations:

$$\nu_{\text{acc}} = \sqrt{\frac{\sum_{j=1}^{p=6} |\nu(c_j) - \nu^{\text{th}}(c_j)|^2}{p - 1}}, \tag{11}$$

$$\Gamma_{\text{acc}} = \sqrt{\frac{\sum_{j=1}^{p=6} |\Gamma(c_j) - \Gamma^{\text{th}}(c_j)|^2}{p - 1}}, \tag{12}$$

with j the index of the concentration. For the TFPI and VIPA (averaged from the results for VIPA1 and VIPA2) we find similar accuracies for the frequency shift, $\nu_{\text{acc}}^{TFPI} = 9.00$ MHz and $\nu_{\text{acc}}^{VIPA} = 11.29$ MHz, respectively. For the linewidth however, we found $\Gamma_{\text{acc}}^{TFPI} = 15.34$ MHz and $\Gamma_{\text{acc}}^{VIPA} = 31.35$ MHz, indicating a lower accuracy for the VIPA measurements.

4. Applications of VIPA-based spectrometer to multicellular spheroids

Given that the VIPA configuration is faster than TFPI under same experimental conditions, a crucial advantage for biological applications, we here use the VIPA spectrometer to probe the mechanics of multicellular tumor spheroids (MCTS). MCTS are engineered from the spontaneous aggregation of two different colorectal carcinoma cell lines (HCT-116 and HT-29, see Methods) that have different cohesive properties, as well as different response to drugs [36]. For these measurements, the microscope is placed inside an incubation chamber to maintain physiological conditions (37°C and 5% CO_2). The microscope is also equipped with a motorized 2-axis stage for fast screening of MCTS in standard 96-well plates, and for imaging purposes. We show an image of a HCT-116 spheroid in Fig. 7(a) with a typical diameter of ~350 μm. For ilustration,
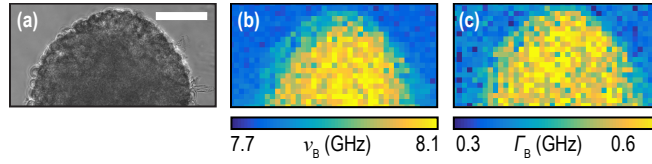
Fig. 7. Optical image (a) of a HCT-116 tumor spheroid and the corresponding maps of (b) the Brillouin frequency shift ν_B, and (c) the Brillouin linewidth Γ_B. Scale bar: 100 μm.
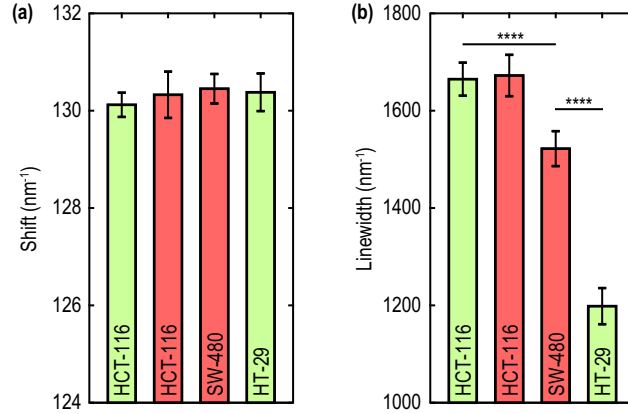

Fig. 8. (a) Brillouin shift and (b) linewidth expressed in wavenumber measured at the center of HCT-116 ($n = 48$) and HT-29 ($n = 45$) spheroids at the 532 nm wavelength used in this paper (green bars). We also reproduce the data from Ref. [16] for HCT-116 ($n = 23$) and SW-480 ($n = 27$) spheroids measured at 647.1 nm (red bars). ★★★★$p < 0.0001$, unpaired two-tailed t tests).

we also show images of the frequency shift ν_B and linewidth Γ_B recorded with a scanning step of 10 μm.

In order to compare the Brillouin signature of the different colorectal cell lines, we performed measurements in the center of HCT-116 and HT-29 spheroids. To compare with data obtained at other wavelengths, we plot the shift and linewidth, expressed in wavenumber, in Figs. 8(a) and 8(b), respectively (green bars). We also reproduce the data from Ref. [16] for HCT-116 and SW-480 spheroids measured at 647.1 nm (red bars). We observe a similar shift for all cell lines, demonstrating that the sound velocity does not vary across these colorectal cell lines. On the other hand, we observe a significant difference in the linewidth ($p < 0.0001$, unpaired two-tailed t tests), allowing to discriminate between the cell lines.

5. Conclusion

In this paper, we have established a protocol to estimate the precision of BLS spectrometers from the standard deviation of repeated measurements in pure water. This study showed that, regardless of the technology of the spectrometer, the precision only depends on the SNR. We have also evaluated the accuracy, for both the frequency shift and the linewidth, from the difference between theory and measurements in saline solutions of increasing concentrations. Our analysis shows that only the acquisition time and laser power required to reach a given SNR should be quoted. This protocol is easy to replicate and can be used across different labs to evaluate the performances of different optical designs.

To demonstrate this, we have coupled two types of BLS spectrometers, based on a VIPA and on a scanned Fabry-Pérot, respectively, to an inverted microscope with temperature control. We have found similar performances in terms of precision and accuracy, but shorter acquisition times for the VIPA-based technology for a given SNR. This comparison suggests that, for applications to biology where throughput is a key parameter, VIPA-based systems could be more suited. It should be mentioned that recent improvements in the design of tandem Fabry-Pérot interferometers have allowed a much higher contrast (about 150 dB) than the commercial model we have used in this paper, which should allow a higher acquisition speed [18]. For illustration, we have imaged multicellular tumor spheroids.

We have compared three classical colorectal cell lines that possess different metastatic potentials and adhesive properties [37]. Our data demonstrates that the spectrometer is sensitive enough to detect significant changes in the linewidth between these cell lines. In particular, HT-29 MCTS showed a lower Γ_B than the other cell lines. HT-29 cells are rich in cadherin/catenin cell-cell junctions providing a cohesive character implicated in 3D drug resistance [36]. This result suggests that BLS measurements of the viscosity could be used as read-out to distinguish different level of drug resistance.

We did not observe any change in the sound velocity, suggesting that, in these spheroid models, the stiffness originates from a universal organisation at the microscale, as already pointed out at the single cell level at GHz frequencies [38]. In future, this observation needs to be reconciled with our observation of varying levels of viscosity, and analyzed in the frame of current poroelastic theories [16, 39].

6.   Acknowledgments

7.   Disclosures

The authors declare that there are no conflicts of interest related to this article.

References

1. M. Urbanska, M. Winzi, K. Neumann, S. Abuhattum, P. Rosendahl, P. Müller, A. Taubenberger, K. Anastassiadis, and J. Guck, "Single-cell mechanical phenotype is an intrinsic marker of reprogramming and differentiation along the mouse neural lineage," Development **144**, 4313–4321 (2017).
2. M. J. Paszek, N. Zahir, K. R. Johnson, J. N. Lakins, G. I. Rozenberg, A. Gefen, C. A. Reinhart-King, S. S. Margulies, M. Dembo, D. Boettiger, D. A. Hammer, and V. M. Weaver, "Tensional homeostasis and the malignant phenotype," Cancer Cell **8**, 241–254 (2005).
3. S. K. Green, G. Francia, C. Isidoro, and R. S. Kerbel, "Antiadhesive antibodies targeting e-cadherin sensitize multicellular tumor spheroids to chemotherapy in vitro," Mol. Cancer Ther. **3**, 149–159 (2004).
4. P. Kollmannsberger and B. Fabry, "Linear and nonlinear rheology of living cells," Annu. Rev. Mater. Res. **41**, 75–97 (2011).
5. E. Moeendarbary, L. Valon, M. Fritzsche, A. R. Harris, D. A. Moulding, A. J. Thrasher, E. Stride, L. Mahadevan, and G. T. Charras, "The cytoplasm of living cells behaves as a poroelastic material," Nat. Mater. **12**, 253–261 (2013).
6. R. K. Jain, "Normalizing tumor microenvironment to treat cancer: Bench to bedside to biomarkers," J. Clin. Oncol. **31**, 2205–2218 (2013).
7. M. Plodinec, M. Loparic, C. A. Monnier, E. C. Obermann, R. Zanetti-Dallenbach, P. Oertle, J. T. Hyotyla, U. Aebi, M. Bentires-Alj, R. Y. H. Lim, and C.-A. Schoenenberger, "The nanomechanical signature of breast cancer," Nat. Nanotechnol. **7**, 757–765 (2012).
8. M. Krieg, G. Fläschner, D. Alsteens, B. M. Gaub, W. H. Roos, G. J. L. Wuite, H. E. Gaub, C. Gerber, Y. F. Dufrêne, and D. J. Müller, "Atomic force microscopy-based mechanobiology," Nat. Rev. Phys. **1**, 41–57 (2019).
9. C. M. Elkins, W.-J. Shen, V. K. Khor, F. B. Kraemer, and G. G. Fuller, "Quantification of stromal vascular cell mechanics with a linear cell monolayer rheometer," J. Rheol. **59**, 33–50 (2015).

10. R. Prevedel, A. Diz-Muñoz, G. Ruocco, and G. Antonacci, "Brillouin microscopy: an emerging tool for mechanobiology," Nat. Methods **16**, 969–977 (2019).

11. G. Scarcelli, W. J. Polacheck, H. T. Nia, K. Patel, A. J. Grodzinsky, R. D. Kamm, and S. H. Yun, "Noncontact three-dimensional mapping of intracellular hydromechanical properties by brillouin microscopy," Nat. Methods **12**, 1132 (2015).

12. T. Dehoux, M. A. Ghanem, O. F. Zouani, J. M. Rampnoux, Y. Guillet, S. Dilhaire, M. C. Durrieu, and B. Audoin, "All-optical broadband ultrasonography of single cells," Sci. Rep. **5**, 8650 (2015).

13. R. Schlüßler, S. Möllmert, S. Abuhattum, G. Cojoc, P. Müller, K. Kim, C. Möckel, C. Zimmermann, J. Czarske, and J. Guck, "Mechanical mapping of spinal cord growth and repair in living zebrafish larvae by brillouin imaging," Biophys. J. **115**, 911–923 (2018).

14. K. Elsayad, S. Werner, M. Gallemí, J. Kong, E. R. Sánchez Guajardo, L. Zhang, Y. Jaillais, T. Greb, and Y. Belkhadir, "Mapping the subcellular mechanical properties of live cells in tissues with fluorescence emission–brillouin imaging," Sci. Signal. **9**, rs5 (2016).

15. T. Lainović, J. Margueritat, Q. Martinet, X. Dagany, L. Blažić, D. Pantelić, M. D. Rabasović, A. J. Krmpot, and T. Dehoux, "Micromechanical imaging of dentin with brillouin microscopy," Acta Biomater. **105**, 214–222 (2020).

16. J. Margueritat, A. Virgone-Carlotta, S. Monnier, H. Delanoë-Ayari, H. C. Mertani, A. Berthelot, Q. Martinet, X. Dagany, C. Rivière, J.-P. Rieu, and T. Dehoux, "High-frequency mechanical properties of tumors measured by brillouin light scattering," Phys. Rev. Lett. **122**, 018101 (2019).

17. S. M. Lindsay, M. W. Anderson, and J. R. Sandercock, "Construction and alignment of a high performance multipass vernier tandem fabry–perot interferometer," Rev. Sci. Instrum. **52**, 1478–1486 (1981).

18. F. Scarponi, S. Mattana, S. Corezzi, S. Caponi, L. Comez, P. Sassi, A. Morresi, M. Paolantoni, L. Urbanelli, C. Emiliani, L. Roscini, L. Corte, G. Cardinali, F. Palombo, J. R. Sandercock, and D. Fioretto, "High-performance versatile setup for simultaneous brillouin-raman microspectroscopy," Phys. Rev. X **7**, 031015 (2017).

19. M. Shirasaki, "Large angular dispersion by a virtually imaged phased array and its application to a wavelength demultiplexer," Opt. Lett. **21**, 366–368 (1996).

20. J. Zhang, X. A. Nou, H. Kim, and G. Scarcelli, "Brillouin flow cytometry for label-free mechanical phenotyping of the nucleus," Lab Chip **17**, 663–670 (2017).

21. Z. Coker, M. Troyanova-Wood, A. J. Traverso, T. Yakupov, Z. N. Utegulov, and V. V. Yakovlev, "Assessing performance of modern brillouin spectrometers," Opt. Express **26**, 2400–2409 (2018).

22. L. Brillouin, "Diffusion de la lumière et des rayons x par un corps transparent homogène," Ann. Phys. **9**, 88–122 (1922).

23. J. Xu, X. Ren, W. Gong, R. Dai, and D. Liu, "Measurement of the bulk viscosity of liquid by brillouin scattering," Appl. Opt. **42**, 6704–6709 (2003).

24. T. A. Litovitz and C. M. Davis, *Physical Acoustics*, vol. 2A (Academic, New York, 1965).

25. C. J. Montrose, V. A. Solovyev, and T. A. Litovitz, "Brillouin scattering and relaxation in liquids," J. Acoust. Soc. Am. **43**, 117–130 (1968).

26. G. Scarcelli and S. H. Yun, "Confocal brillouin microscopy for three-dimensional mechanical imaging," Nat. Photonics **2**, 39–43 (2008).

27. G. Antonacci, M. R. Foreman, C. Paterson, and P. Török, "Spectral broadening in brillouin imaging," Appl. Phys. Lett. **103**, 221105 (2013).

28. Z. Meng and V. V. Yakovlev, "Precise determination of brillouin scattering spectrum using a virtually imaged phase array (vipa) spectrometer and charge-coupled device (ccd) camera," Appl. Spectrosc. **70**, 1356–1363 (2016).

29. S. Smith, *Special Imaging Techniques* (Elsevier Science, 2013), chap. 25, Demystifying technology series.

30. V. A. Del Grosso and C. W. Mader, "Speed of sound in pure water," J. Acoust. Soc. Am. **52**, 1442–1446 (1972).

31. S. J. Kleis and L. A. Sanchez, "Dependence of sound velocity on salinity and temperature in saline solutions," Sol. Energy **46**, 371–375 (1991).

32. N. Bilaniuk and G. S. K. Wong, "Speed of sound in pure water as a function of temperature," J. Acoust. Soc. Am. **93**, 1609–1612 (1993).

33. C.-Y. Tan and Y.-X. Huang, "Dependence of refractive index on concentration and temperature in electrolyte solution, polar solution, nonpolar solution, and protein solution," J. Chem. Eng. Data **60**, 2827–2833 (2015).

34. S. V. Adichtchev, Y. A. Karpegina, K. A. Okotrub, M. A. Surovtseva, V. A. Zykova, and N. V. Surovtsev, "Brillouin spectroscopy of biorelevant fluids in relation to viscosity and solute concentration," Phys. Rev. E **99**, 062410 (2019).

35. D. Lide, *CRC handbook of chemistry and physics* (CRC Press, Boca Raton, 1999).

36. A. Virgone-Carlotta, M. Lemasson, H. C. Mertani, J.-J. Diaz, S. Monnier, T. Dehoux, H. Delanoë-Ayari, C. Rivière, and J.-P. Rieu, "In-depth phenotypic characterization of multicellular tumor spheroids: Effects of 5-fluorouracil," PLOS ONE **12**, e0188100 (2017).

37. M. El-Bahrawy, S. R. Poulsom, A. J. Rowan, I. T. Tomlinson, and M. R. Alison, "Characterization of the e-cadherin/catenin complex in colorectal carcinoma cell lines," Int. J. Exp. Pathol. **85**, 65–74 (2004).

38. O. F. Zouani, T. Dehoux, M.-C. Durrieu, and B. Audoin, "Universality of the network-dynamics of the cell nucleus at high frequencies," Soft Matter **10**, 8737–8743 (2014).

39. P.-J. Wu, I. V. Kabakova, J. W. Ruberti, J. M. Sherwood, I. E. Dunlop, C. Paterson, P. Török, and D. R. Overby, "Water content, not stiffness, dominates brillouin spectroscopy measurements in hydrated materials," Nat. Methods **15**, 561–562 (2018).